Available online at www.sciencedirect.com
SCIENCE DIRECT
Acta Materialia 54 (2006) 3637–3646
Acta MATERIALIA
www.actamat-journals.com

Glass-forming ability and stability of ternary Ni-early transition metal (Ti/Zr/Hf) alloys

Joysurya Basu, S. Ranganathan *

Department of Metallurgy, Indian Institute of Science, Bangalore 560 012, India

Received 19 December 2004; received in revised form 22 January 2006; accepted 23 January 2006

Abstract

Four Ni-bearing Ti, Zr and Hf ternary alloys of nominal composition $Zr_{41.5}Ti_{41.5}Ni_{17}$, $Zr_{25}Ti_{25}Ni_{50}$, $Zr_{41.5}Hf_{41.5}Ni_{17}$ and $Ti_{41.5}Hf_{41.5}Ni_{17}$ were rapidly solidified in order to produce ribbons. The Zr–Ti–Ni and Ti–Hf–Ni alloys become amorphous, whereas the Zr–Hf–Ni alloy shows precipitation of a cubic phase. The devitrification of all three alloys was followed and the relative tendency to form nanoquasicrystals and cF96 phases analysed. The relative glass-forming ability of the alloys can be explained by taking into account their atomic size difference. Addition of Ni often leads to quasicrystallisation or quasicrystal-related phases. This can be explained by the atomic radius and heat of mixing of the constituent elements. The phases precipitated at the initial stages of crystallisation indicate the possible presence of Frank–Kasper polyhedral structure in the amorphous alloys. Structural analysis reveals that the Laves and the anti-Laves phases have the same polyhedral structural unit, which is similar to the structural characteristics of glass.

Keywords: Metallic glasses; Transition metals; Crystallisation; Quasicrystals; Laves phases

1. Introduction

Since the discovery of bulk metallic glasses, Zr-based alloys have been much studied [1]. These alloys can be classified into two groups depending on the alloying constituents. The first is Zr and Al with transition metals in which Cu and Ni are very important alloying additions. The second class of alloys is synthesised with transition metals without Al. In this second category of alloys, Zr can be partially or fully replaced by Hf and Ti to obtain quaternary and higher order alloys. The addition of Pd, Pt, Au and Ag introduces nanoquasicrystallisation [2]. In several systems amorphous phase separation can also be observed [3].

In binary phase diagrams of Zr, Ti and Hf with Ni, a number of deep eutectics and intermetallics are present and glasses form over a wide composition range [4]. Isomorphous substitution of Zr by Hf does not change the local structure of the glass, as crystalline $NiZr_2$ and $NiHf_2$ are isomorphous [5]. For ternary alloys glass formation in Ti–Hf–(Ni/Cu), Zr–Hf–Ni and Zr–Ti–(Ni/Cu) systems has been reported [6]. Also, glasses form in Hf–Cu–Ni, Zr–Cu–Ni and Ti–Cu–Ni systems [7]. Among ternary alloys, Zr–Ti–Ni is the most widely studied system. Both metastable and stable quasicrystals have been reported to occur in this system depending on the alloy composition. Icosahedral quasicrystalline phase forms after annealing by solid-state transformation of hexagonal Laves phase and body-centred cubic solid solution phase β-(Ti–Zr), the primary solidification product directly from the liquid. Annealing at lower temperature improves the structural quality of the quasicrystals. Annealing at higher temperature gives rise to 1/1 approximant phase [8]. The phase transformation of this alloy is complex and all phase transformations can be avoided to produce an amorphous phase by non-equilibrium processing techniques. In the Ti–Hf–Ni system a similar quasicrystal and rational approximant has been reported [9]. The Zr–Hf–Ni system has not received much attention in this context. Indeed this system is likely to

* Corresponding author.
E-mail address: rangu@met.iisc.ernet.in (S. Ranganathan).

1359-6454/$30.00
doi:10.1016/j.actamat.2006.01.043

show a very different behaviour, as for all practical purposes the entire ternary diagram can be treated as pseudo-binary sections as many binary intermetallics are common in Zr–Ni and Hf–Ni. Glass formation in quaternary and quinary alloys containing Zr, Ti, Hf, Cu and Ni has also been reported [10]. Quinary Zr–Ti–Hf–Cu–(Fe/Co/Ni) can be cast in a copper mould in the form of 1.5 mm diameter rods with equal amounts of the elements. Though there is no specific host element, the good glass-forming ability of the alloy is because of the presence of a large number of elements [11]. Recently Kim et al. [12] have studied the glass-forming ability of Zr–Ti–Hf–Cu–Ni alloys with substitution of Al over a composition range. It has been observed that the substitution of Cu and Ni with Al improves the glass-forming ability, but beyond a certain limit the glass-forming ability decreases. Good glass-forming ability in the quaternary Ti–Zr–Ni–Cu system has been reported [13] and Hf–Cu–Ni–Al alloy can be cast in the form of 3 mm diameter rods by copper mould casting [14].

In the (Zr, Ti, Hf)–(Cu, Ni) system, it is possible to design six binary, six ternary and two quaternary alloy systems either with Cu or with Ni. Though there is a large number of reports on nanocrystallisation and nanoquasicrystallisation in Zr-based alloys, the structural origin of nanoquasicrystals and structurally complex intermetallic phases is still not properly understood. A complete understanding of the glass formation and crystallisation behaviour of ternary (Zr, Ti, Hf)–(Cu, Ni) alloys will be helpful in rationalising the behaviour of the alloys, which can be extended to the relatively complex quaternary and quinary alloys. The aim of this work is to investigate the crystallisation behaviour of different ternary alloy systems and to understand the glass-forming and quasicrystal-forming ability of different alloys. In this work only ternary Ni-bearing alloys are considered. Cu-bearing alloys will be considered in a companion paper.

2. Experimental

Four alloys belonging to three ternary Ni-bearing alloy systems, Zr–Ti–Ni, Zr–Hf–Ni and Ti–Hf–Ni, were studied. Three of the alloys have identical Ni contents and the other is rich in Ni. The alloy systems along with the composition of the alloys are given in Table 1.

Four alloys of the nominal compositions were fabricated by melting pure Zr (99.99%), Ti (99.99%), Hf (99.99%) and Ni (99.99%) in appropriate proportions in a vacuum arc melting furnace with backfilled argon gas. The alloys were re-melted several times in order to ensure their compositional homogeneity. The alloys were then melt-spun in a single-roller melt-spinning unit at a wheel speed of 40 m s^{-1} in an argon atmosphere. The melt-spun ribbons were approximately 5 mm in width and 50–60 μm in thickness.

Table 1
Alloy systems and their compositions

Alloy system	Composition (at.%)
Zr–Ti–Ni	$Zr_{41.5}Ti_{41.5}Ni_{17}$
	$Zr_{25}Ti_{25}Ni_{50}$
Zr–Hf–Ni	$Zr_{41.5}Hf_{41.5}Ni_{17}$
Ti–Hf–Ni	$Ti_{41.5}Hf_{41.5}Ni_{17}$

The melt-spun ribbons were characterised using a JEOL JDX 8030 X-ray diffractometer with Cu Kα radiation and a JEOL 2000 FX II transmission electron microscope operated at 200 kV. The thermal stability and transformation behaviour of the ribbons were studied using differential scanning calorimetry (DSC; Mettler Toledo 822E). To study the phase evolution, the ribbons were heat treated at the peak temperatures indicated by DSC and just below the first crystallisation temperature for 10 min and then water quenched. To ascertain the stability of the phases the ribbons were heat treated at the peak temperature indicated by DSC and just below the first crystallisation temperature for 4 h and then furnace cooled. Before each heat treatment the ribbons were sealed in a quartz tube under vacuum in order to avoid oxidation. The heat-treated samples were characterised using X-ray diffraction (XRD) and transmission electron microscopy (TEM).

3. Results

3.1. Zr–Ti–Ni alloy

In the XRD pattern of the $Zr_{41.5}Ti_{41.5}Ni_{17}$ alloy melt-spun at 40 m s^{-1} wheel speed (Fig. 1(a)) no peak corresponding to any crystalline phase can be seen. The diffuse diffraction hump over the angular range 30–40° confirms the presence of an amorphous phase in the melt-spun ribbon. TEM study of the same alloy does not reveal the presence of any crystalline phase. The presence of a diffuse halo in the electron diffraction pattern further confirms the amorphous nature of the alloy. From the DSC thermogram of the alloy (Fig. 2(a)), it can be observed that the crystallisation behaviour of the alloy is complex, as it occurs in three distinct exothermic events. The peak temperatures for these three exothermic events are 810, 880 and 930 K. These temperatures, as well as 700 K, which is below the first crystallisation peak temperature, have been taken as the heat treatment temperatures.

From the XRD patterns of the $Zr_{41.5}Ti_{41.5}Ni_{17}$ alloy melt-spun at 40 m s^{-1} wheel speed and heat treated at 700, 810, 880 and 930 K for 10 min (Fig. 3(a)–(d)), it can be observed that the alloy starts crystallising even after the heat treatment below the first crystallisation peak temperature. The diffraction pattern after heat treatment at 700 K matches that of an icosahedral quasicrystalline phase reported in previous literature. The quasicrystalline particles are very fine, as can be ascertained from the peak broadening in the diffraction pattern. After heat treatment at 810 K for 10 min the peak positions do not change. Only the peak intensity increases and the peak becomes sharper. After heat treatment at 880 K, a number of sharp peaks

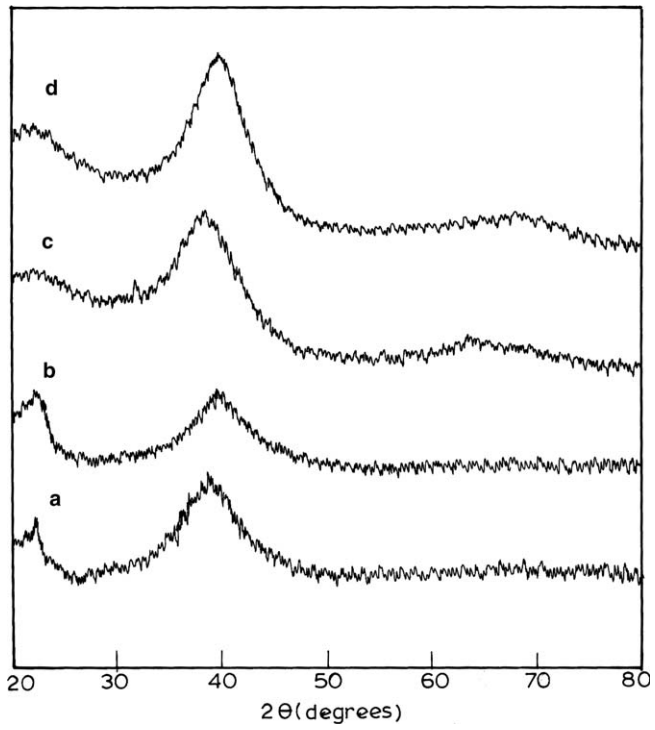

Fig. 1. XRD patterns of: (a) the $Zr_{41.5}Ti_{41.5}Ni_{17}$ and (b) the $Zr_{25}Ti_{25}Ni_{50}$ alloy melt-spun at 40 m s^{-1} wheel speed. Both the alloys are amorphous after melt spinning.

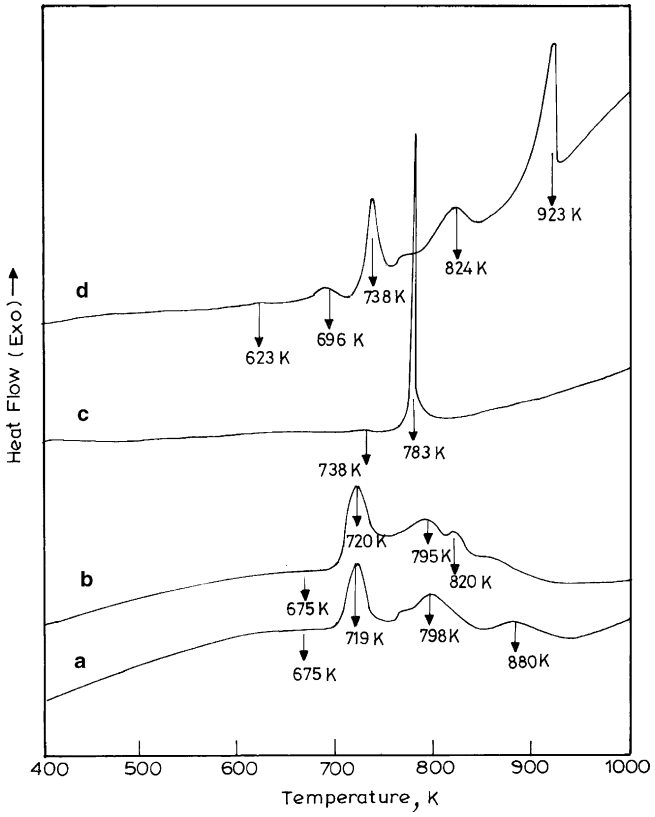

Fig. 2. DSC thermograms of: (a) $Zr_{41.5}Ti_{41.5}Ni_{17}$, (b) $Zr_{25}Ti_{25}Ni_{50}$, (c) $Zr_{41.5}Hf_{41.5}Ni_{17}$ and (d) $Ti_{41.5}Hf_{41.5}Ni_{17}$ melt-spun at 40 m s^{-1} wheel speed.

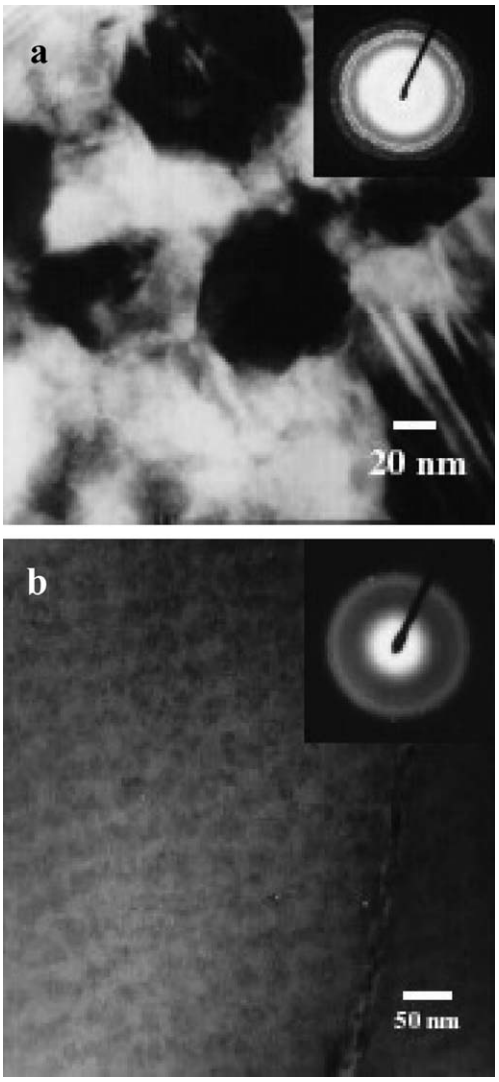

Fig. 3. XRD patterns of the $Zr_{41.5}Ti_{41.5}Ni_{17}$ alloy melt spun at 40 m s^{-1} wheel speed and heat treated at: (a) 700 K, (b) 810 K, (c) 880 K and (d) 930 K for 10 min. After crystallisation cF96 $NiZr_2$, oC68 $Ni_{10}Zr_7$ and oC8 NiZr phases can be observed.

can be seen. These peaks can be indexed to cF96 $NiZr_2$ phase with a lattice parameter of 12.27 Å. After heat treatment at 930 K for 10 min the alloy becomes totally crystalline, as is evident from the diffraction pattern. At this stage, apart from the cF96 $NiZr_2$ phase, oC8 NiZr and oC68 $Ni_{10}Zr_7$ phases can also be seen.

TEM study of the alloy after heat treatment at 700 K for 4 h also reveals nanoquasicrystallisation. The TEM image and electron diffraction patterns of the alloy after heat treatment at 810 K for 4 h are shown in Fig. 4(a). After heat treatment at 810 K nearly spherical precipitates varying size in the range 50–100 nm can be observed in the amorphous matrix. In the diffraction patterns quasicrystalline 5-, 3- and 2-fold symmetries of the precipitates can be observed. The convergent beam electron diffraction pattern showing the 5-fold symmetry is shown in the inset of Fig. 4(a). It can be concluded that after heat treatment at this temperature, nanoquasicrystals are precipitated in the

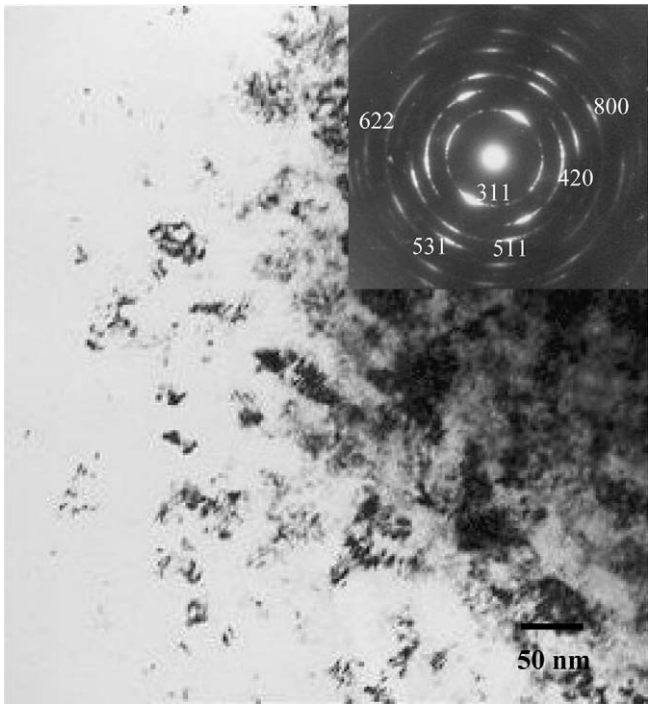

Fig. 4. TEM images and electron diffraction patterns of: (a) $Zr_{41.5}Ti_{41.5}Ni_{17}$ melt-spun at 40 m s^{-1} wheel speed and heat treated at 810 K for 4 h and (b) $Zr_{25}Ti_{25}Ni_{50}$ melt-spun at 40 m s^{-1} wheel speed and heat treated at 733 K for 10 min. Quasicrystallisation in $Zr_{41.5}Ti_{41.5}Ni_{17}$ and precipitation of cF96 Zr_2Ni phase in $Zr_{25}Ti_{25}Ni_{50}$ alloy can be observed.

amorphous matrix and they are stable up to 4 h of annealing treatment at this temperature. After annealing at 880 K for 4 h the precipitates grow to the size of 100–300 nm and they are faceted or polygonal in shape. From the diffraction pattern the presence of the cF96 $NiZr_2$ phase can be confirmed. After heat treatment at 930 K the grains grow to about 1 μm in size and bend contours can be seen in the grains. The grains are faceted. The analysis of the diffraction pattern reveals the presence of cF96 $NiZr_2$, oC8 NiZr and oC68 $Ni_{10}Zr_7$ phases.

In the XRD pattern of the $Zr_{25}Ti_{25}Ni_{50}$ alloy melt-spun at 40 m s^{-1} wheel speed (Fig. 1(b)), no peak corresponding to any crystalline phase can be seen. The diffraction hump over the angular range of 30–40° indicates the amorphous nature of the alloy after melt spinning. The DSC thermogram of the alloy (Fig. 2(b)) shows that the crystallisation behaviour of the alloy is relatively simple and occurs as a single exothermic event, though a small exothermic hump can be seen just before the major heat event. The peak temperature of the major heat event is 783 K.

The TEM image and the convergent beam electron diffraction pattern of the $Zr_{25}Ti_{25}Ni_{50}$ alloy heat treated at 733 K for 10 min is shown in Fig. 4(b). In the micrograph, faceted precipitates of 20–30 nm in size are seen in the amorphous matrix. The convergent beam electron diffraction pattern can be indexed to the [1 1 1] type zone axis of face-centred cubic (fcc) lattice. The calculated lattice parameter is 11.56 Å, which is very close to that of the cF96 Ti_2Ni phase reported in the literature. Probably non-stoichiometry and the presence of Zr in the alloy lead to the observed change in the lattice parameter.

3.2. Zr–Hf–Ni alloy

In the XRD pattern of the $Zr_{41.5}Hf_{41.5}Ni_{17}$ alloy melt-spun at 40 m s^{-1} wheel speed, a sharp crystalline peak can be seen. The peak cannot be indexed with certainty with any known crystalline phase in this system. The TEM image and the corresponding electron diffraction pattern of the same alloy (Fig. 5(a)) show that the microstructure of the alloy after melt spinning is not uniform. Though a considerable amount of amorphous phase is present in the alloy after melt spinning, densely populated crystallites can be seen in localised regions. The precipitates are dendritic in nature and their size varies in the range 50–100 nm. From the convergent beam electron diffraction pattern with a larger spot size, shown in the inset, the presence of the amorphous phase can be confirmed from the

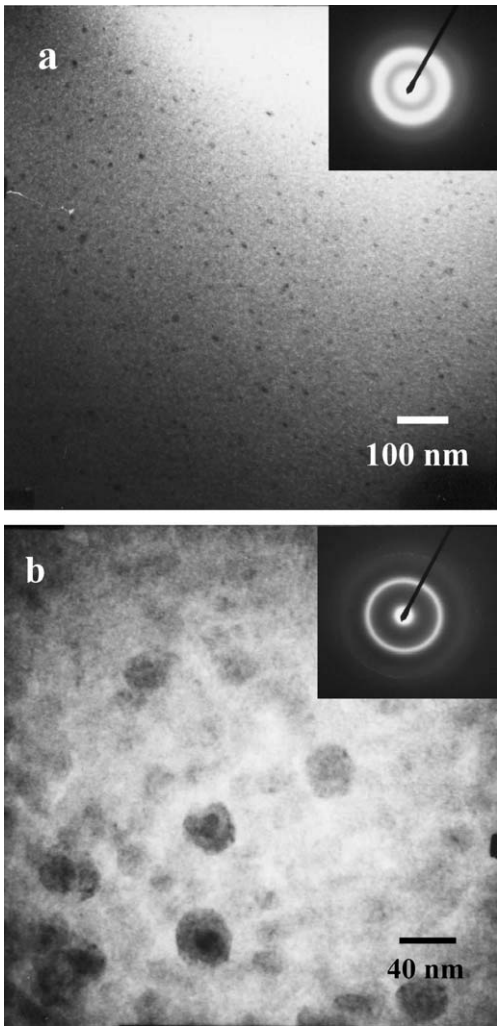

Fig. 5. TEM images and electron diffraction patterns of: (a) $Zr_{41.5}Hf_{41.5}Ni_{17}$ and (b) $Ti_{41.5}Hf_{41.5}Ni_{17}$ melt-spun at 40 m s^{-1} wheel speed. While the $Ti_{41.5}Hf_{41.5}Ni_{17}$ alloy is amorphous, precipitation of a cubic phase in the amorphous matrix is seen in the $Zr_{41.5}Hf_{41.5}Ni_{17}$ alloy.

diffuse halo. The spots in the diffraction pattern conform to the [0 0 1] pattern of a fcc phase. The lattice parameter of the phase is 5.02 Å. This observation substantiates the fact that the alloy is not totally amorphous after melt spinning and the microstructure is inhomogeneous in nature. Due to this inhomogeneity, the presence of the amorphous phase is masked in the diffraction pattern. The peaks in the XRD pattern can be indexed as fcc with lattice parameter of 5.02 Å. The DSC thermogram of the $Zr_{41.5}Hf_{41.5}Ni_{17}$ alloy after melt spinning at 40 m s^{-1} is shown in Fig. 2(c). The alloy crystallises in a single exothermic event, though a small diffuse exothermic hump is seen just before the main exothermic event. The peak temperature of the main crystallisation event is 728 K. The melt-spun alloy was therefore heat treated at 653 and 728 K in order to study the phase evolution during crystallisation.

The XRD patterns of the $Zr_{41.5}Hf_{41.5}Ni_{17}$ alloy after heat treatment at 653 and 728 K for 10 min are shown in Fig. 6. It is evident that the alloy starts crystallising below the first crystallisation peak temperature. After heat treatment at 653 K only one peak in the diffraction pattern can be seen. The peak position is the same as that for the melt-spun alloy. Thus it can be concluded that the same fcc phase precipitates after heat treatment at 653 K. After heat treatment at 728 K the alloy becomes totally crystalline and a number of peaks can be seen in the diffraction pattern. Analysis of the diffraction pattern reveals the presence of the same fcc phase along with tI12 $Ni(Zr,Hf)_2$ and oC8 Ni(Zr, Hf) phases. Though $NiZr_2$, $NiHf_2$ and NiZr, NiHf are different intermetallics, they are isostructural and the lattice parameters of the phases are very similar. As the atomic sizes of Zr and Hf are close, it is possible to substitute one for another. TEM images and corresponding electron diffraction patterns of the $Zr_{41.5}Hf_{41.5}Ni_{17}$ alloy after heat treatment at 653 and 728 K reveal that after heat treatment at 653 K the volume fraction of the fcc phase increases. At this stage the size of the precipitates varies in the range 50–100 nm and they are spherical or polygonal in shape. The analysis of the diffraction pattern reveals the presence of the fcc phase only. After heat treatment at 728 K two morphologically different types of precipitates can be seen. One type is spherical or polygonal and the other type exhibits a mottled contrast. Electron diffraction patterns reveal the presence of the same cubic phase with 5.02 Å lattice parameter along with $Ni(Zr,Hf)_2$ and Ni(Zr, Hf) phases. The cubic phase does not match with any of the known intermetallics in the relevant system and needs further investigation.

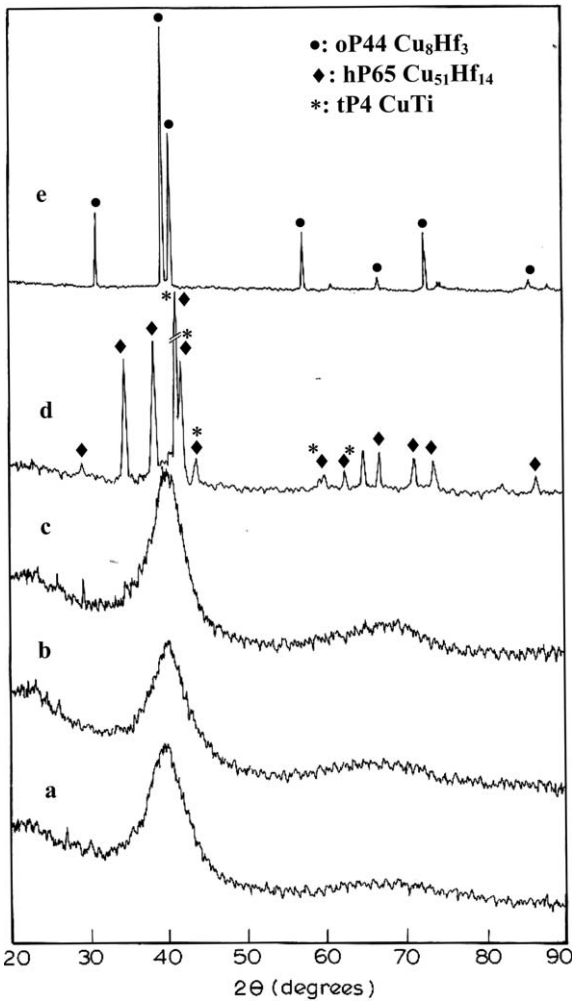

Fig. 6. XRD patterns of the $Zr_{41.5}Hf_{41.5}Ni_{17}$ alloy melt-spun at 40 m s^{-1} wheel speed and heat treated at: (a) 653 K and (b) 728 K for 10 min. Apart from the fcc phase, the tI12 $Ni(Zr,Hf)_2$ and oC8 Ni(Zr, Hf) phases are observed after complete crystallisation.

3.3. Ti–Hf–Ni alloy

The TEM image and electron diffraction pattern of the $Ti_{41.5}Hf_{41.5}Ni_{17}$ alloy melt-spun at 40 m s^{-1} wheel speed are shown in Fig. 5(b). In the micrograph, no contrast from any crystalline phase can be seen and the amorphous nature of the alloy can be confirmed from the diffuse halo in the diffraction pattern. In the DSC thermogram of the alloy, shown in Fig. 2(d), one diffuse exothermic event can be observed over a temperature range of 50 K. The peak starts at 669 K and ends at 716 K. The alloy was heat treated at 548, 648 and 698 K for 10 min.

In the TEM image of the $Ti_{41.5}Hf_{41.5}Ni_{17}$ alloy heat treated at 548 K for 10 min (Fig. 7) very fine precipitates varying in the size range 20–30 nm can be seen in the amorphous matrix. The precipitates are irregular in shape. The convergent beam electron diffraction pattern from the precipitates (Fig. 7 inset) clearly shows the cubic symmetry. The pattern can be indexed to the [0 0 1] type zone axis pattern of a fcc lattice. The calculated lattice parameter is 11.56 Å, which is very close to that of the cF96 Ti_2Ni type phase, reported in the literature. It can be inferred from this observation that after heat treatment the cF96 Ti_2Ni phase is precipitated in the amorphous matrix and the observed variation in the lattice parameter can be attributed to the non-stoichiometry and the presence of Hf in the alloy. The same cF96 phase is seen after heat treatments at 648 and 698 K for 10 min.

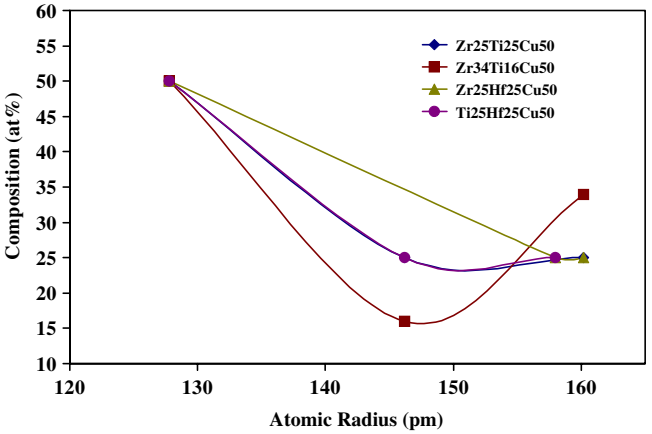

Fig. 7. TEM image and electron diffraction pattern of the $Ti_{41.5}Hf_{41.5}Ni_{17}$ alloy melt-spun at 40 m s^{-1} wheel speed and heat treated at 548 K for 10 min. The diffraction pattern conforms to the [0 0 1] zone axis pattern of the cF96 Ti_2Ni phase.

4. Discussion

The results obtained for the four different alloys belonging to three different alloy systems provide information about their glass-forming ability, quasicrystal-forming ability and crystallisation behaviour. It is possible to rationalise their behaviour in terms of the atomic radii, heat of mixing and phase diagram information. Different features are discussed in the following.

4.1. Glass-forming ability

The composition and the constituent elements were changed systematically in order to draw comparisons. All alloys were synthesised under the same experimental conditions. Both the Zr–Ti–Ni alloys become amorphous after melt spinning at 40 m s^{-1} wheel speed. When Ti is replaced by Hf in the Zr–Hf–Ni alloy, the glass-forming ability decreases. Zr–Hf–Ni alloy precipitates a cubic phase with a lattice parameter of 5.02 Å in the amorphous matrix. Precipitation of a cubic phase in the amorphous matrix with a lattice parameter of 5.3 Å has been reported in Hf–Ni–Cu–Al–Ti alloy [15]. It is not confirmed whether these two phases with different lattice parameter arise from a similar intermetallic. The Ti–Hf–Ni alloy is also amorphous after melt spinning. Ti, Zr and Hf appear in the same group in the periodic table. However, replacement of Ti by Hf leads to a certain change in the glass-forming ability of the alloy. The difference in behaviour can be understood by taking into consideration the atomic size mismatch and binary heat of mixing values. The atomic radii mismatch and binary heat of mixing between Ti, Zr, Hf and Ni are given in Table 2.

It is observed from Table 2 that the atomic radii mismatches of Ti, Zr or Hf with Ni are 15%, 22% and 21%, respectively, and the atomic radii mismatches of Ti and Hf with Zr are 9% and 1%, respectively. The heats of mixing of Ti, Zr and Hf with Ni are highly negative. As the atomic size difference between Zr and Hf is small in comparison to that between Zr and Ti, the replacement of Ti by Hf does not add to the glass-forming ability of the system. In this regard the Zr–Hf–Ni system does not strictly follow Inoue's criteria of glass formation. The Mendeleev number can be introduced to classify the elements [16]. A plot of Mendeleev number with the atomic radii of the elements is shown in Fig. 8. It is seen from the plot that the lanthanides, early transition metals, late transition metals, Be and B occupy different locations in the plot. This plot also helps one to distinguish between elements according to their outer electron configuration.

Table 2
Atomic radii mismatch (%) and binary heat of mixing (kJ mol^{-1}) of Ti, Zr, Hf, and Ni

	Ti	Zr	Hf	Ni
Atomic radii mismatch				
Ti		9	7	15
Zr			1	22
Hf				21
Heat of mixing				
Zr	0			
Hf	0	0		
Ni	−35	−49	−42	

The behaviour of Ti, Zr and Hf with Ni can further be understood from phase diagram information. All the three binaries Ti–Ni, Zr–Ni and Hf–Ni feature deep eutectics. It is worth noting that Zr–Ni and Hf–Ni form many more intermetallics than Ti–Ni, indicating a close similarity between Zr and Hf and a difference from Ti. This is basically due to the large size difference of Zr and Hf with Ti. In the ternary Zr–Ti–Ni system one important ternary intermetallic phase is NiTiZr, which is a ternary hexagonal Laves phase with hP12 structure. This intermetallic phase is present in the $NiTi_2$–$NiZr_2$ vertical section. In the vertical section of $NiTi_2$–$NiZr_2$ two eutectics can be seen and the mutual solubility of $NiTi_2$ and $NiZr_2$ is not very high. It is worth noting that in this vertical section the ternary Laves phase exists, though neither $NiTi_2$ nor $NiZr_2$ is a Laves phase. Though the stoichiometry of $NiZr_2$ and $NiTi_2$ is just opposite to that of the Laves phase, their binary vertical section features NiTiZr ternary Laves phase, where Ti and Ni occupy the same lattice site. It can be concluded from this observation that it is the occupancy of the Ti atoms that leads to the structure formation. A similar trend occurs for the Ti–Hf–Ni system [17]. Very little information is available about the ternary phase diagram of the Zr–Hf–Ni system. Until now no ternary Laves phase has been found in this system [18].

The atomic size distribution plot has received considerable attention recently, so far as glass-forming ability is concerned. It is postulated that the concave upward shape of the plot is the most favourable one for the formation of bulk metallic glass [19]. The atomic size distribution plots of the alloys studied in the present work are shown in Fig. 9. It is seen from the Zr–Ti–Ni alloys that none of the plots is

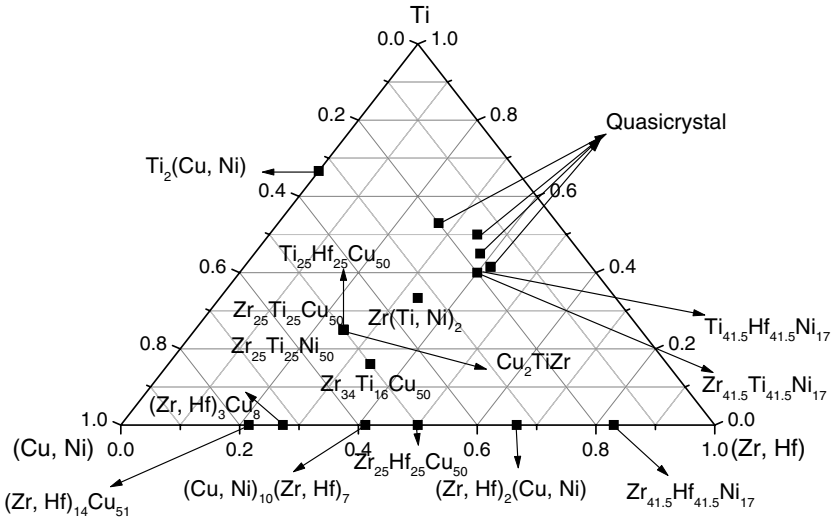

Fig. 8. Mendeleev number vs. atomic size distribution plot. Mendeleev number can distinguish between elements depending on their electronic structure.

predominantly concave upward. The same is also true for the Zr–Hf–Ni and Ti–Hf–Ni alloys, though a large difference in the atomic size can be discerned. The shape of the curves can be made concave upward by suitably choosing the alloying constitution but that does not ensure any composition with better glass-forming ability. This plot can be used to deduce how widely apart the atomic size of the constituent elements are, and dividing the atomic size of the elements into large, medium and small category may be helpful in choosing a proper alloy system.

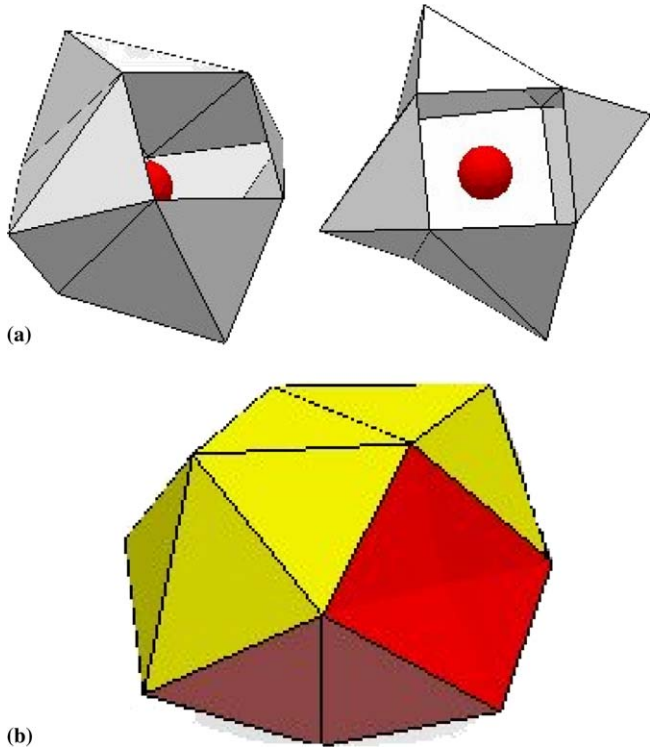

Fig. 9. Atomic size distribution plots of $Zr_{41.5}Ti_{41.5}Ni_{17}$, $Zr_{25}Ti_{25}Ni_{50}$, $Zr_{41.5}Hf_{41.5}Ni_{17}$ and $Ti_{41.5}Hf_{41.5}Ni_{17}$. None of the curves is concave upward.

4.2. Crystallisation behaviour

The $Zr_{41.5}Ti_{41.5}Ni_{17}$ alloy crystallises in three exothermic events, whereas the $Zr_{25}Ti_{25}Ni_{50}$ alloy crystallises in a single exothermic event. The Zr–Hf–Ni alloy crystallises in a single exothermic event and the Ti–Hf–Ni alloy exhibits a diffuse exothermic event spanning 50 K. The $Zr_{41.5}Ti_{41.5}Ni_{17}$ alloy at the initial stages of crystallisation precipitates an icosahedral quasicrystalline phase, which in the later stages of annealing transforms to the cF96 $NiZr_2$ phase. Prolonged heat treatment results in the precipitation of oC8 NiZr and oC68 $Ni_{10}Zr_7$ phases. The quasicrystalline phase is stable up to 4 h of annealing treatment at the peak temperature, as indicated by the DSC results. The amorphous $Zr_{25}Ti_{25}Ni_{50}$ alloy precipitates cF96 Ti_2Ni type phase upon heat treatment. The Zr–Hf–Ni alloy precipitates the same cubic phase with a lattice parameter of 5.02 Å after heat treatment, and at the later stages of crystallisation tI12 $Ni(Zr,Hf)_2$ and oC8 Ni(Zr, Hf) phases are also seen. The $Ti_{25}Hf_{25}Ni_{50}$ alloy precipitates the same cF96 Ti_2Ni type phase upon heat treatment. The observed variation in the lattice parameter can be attributed to non-stoichiometry and the presence of Hf in the alloy. Ni with Zr, Hf and Ti produces amorphous, quasicrystalline, complex crystalline and crystalline phases. The quasicrystalline phase formed with Ti and Ni can further be stabilised by oxygen. The $Zr_{41.5}Ti_{41.5}Ni_{17}$ and the $Ti_{41.5}Hf_{41.5}Ni_{17}$ alloys lie very close to the quasicrystal-forming composition reported in the respective systems. In the $Zr_{41.5}Ti_{41.5}Ni_{17}$ alloy quasicrystallisation has been observed.

4.3. Structure and quasicrystallisation

In the present work the compositions of the alloys were changed in order to study the effect of alloying elements. The $Zr_{25}Ti_{25}Ni_{50}$ alloy can be termed a Ni-based alloy. At the same time it can be termed a Zr-based alloy as it is the largest element and contributes most towards glass

formation. The Zr–Ti–Ni alloy precipitates an icosahedral quasicrystalline phase, which can be attributed to the presence of icosahedral clusters in the amorphous alloy due to the favourable atomic size difference. This alloy on further heat treatment precipitates the cF96 Zr_2Ni phase, which has distorted icosahedral clusters. The $Zr_{25}Ti_{25}Ni_{50}$ and $Ti_{41.5}Hf_{41.5}Ni_{50}$ alloys precipitate cF96 Ti_2Ni type phase, which also has icosahedral clusters in it. From the above consideration it can be realised that all the phases can be considered as Frank–Kasper phases, the basic unit of which is the tetrahedron.

It can be inferred from the present study that Frank–Kasper phases exist in this class of amorphous alloys. In some cases they form icosahedral quasicrystals. Under which conditions quasicrystallisation occurs in glass are not totally understood. Inoue et al. [20] have proposed that for a multicomponent alloy system, atomic radii mismatch preferably over 10% and a mixture of atomic pairs with negative and positive or zero enthalpy of mixing among the main constituent elements favour quasicrystallisation. Li et al. [21] have proposed that a high negative heat of mixing and atomic size difference are the two controlling factors influencing quasicrystallisation. Recently Murty et al. [22] have proposed that a high negative heat of mixing stabilises the liquid and in turn stabilises the Frank–Kasper polyhedra in the liquid. Along with that, the existence of a number of rational approximant structures favours quasicrystallisation. In this proposition the role of atomic size has been totally ignored. In the light of the present work and from published data in the literature, a more conclusive proposition can be extended which clearly brings out the role of atomic size. An icosahedron is a 12-coordination polyhedron. If a small atom sits at the centre and 12 larger atoms sit at the vertices of the icosahedron then in order to form a topologically perfect icosahedron the atomic size difference should be 10%. In the Zr–Ti–Ni system quasicrystallisation can be observed and in this system the atomic size difference between Ti and Ni is 15%. Zr–Cu–Ni–Al alloys when alloyed with Pd, Pt, Au and Ag form quasicrystals [2]. The atomic size difference between Zr with Pt, Au and Ag is between 10% and 15%. The effect of Ti on quasicrystallisation in Zr–Cu–Ni–Al alloy is well documented in the literature [23]. Here again the atomic size difference between Ti and Ni favours quasicrystallisation. Quasicrystallisation in Hf–Pd [24] alloy has been reported. The atomic size difference between Hf and Pd is within 10–15%. It can be inferred from the above discussion that an atomic size difference of 10–15% between a pair of constituent elements, which is close to the ideal value, favours quasicrystallisation. It can be seen that Cu also has a favourable atomic size difference with Ti. As the heat of mixing of Cu with Ti is not highly negative, it cannot form quasicrystals. It can be concluded that a high negative heat of mixing and atomic size difference of 10–15%, which is close to ideal value, favours quasicrystallisation in glasses.

4.4. Laves and anti-Laves phases

The Laves phase is known to be a purely size-factor compound which forms at the atomic size ratio of 1.225. The general formula for a Laves phase is AB_2 where A represents a large atom and B represents a small atom. Two types of Laves phase can be distinguished: cubic and hexagonal. Typical examples are cF24 $MgCu_2$ and hP12 $MgZn_2$, respectively. The space group symmetry for the cubic Laves phase is Fd-3m and that for the hexagonal Laves phase is $P6_3/mmc$. According to the symmetry element $MgNi_2$ has the same space group symmetry as that of $MgZn_2$ with Pearson symbol hP24. Ideally, a Laves phase can be seen as a Frank–Kasper phase. In the cubic Laves phase, four tetrahedral voids are filled by four atoms and four other tetrahedral voids are filled with four regular tetrahedra. Another way of looking at the structure is a close packing of an Archimedian solid with four hexagonal faces and four triangular faces. The solids share the hexagonal faces and the voids are filled with regular tetrahedra. In this arrangement the co-ordination number of the central atom is 16 and that for the vertex atom is 12. The structure of Laves phase can also be explained using the super-tetrahedron model (Fig. 10). In $MgCu_2$ type structure the Mg atoms form a tetrahedron and around each Mg atom an icosahedron is formed which is known as the super-tetrahedron. This super-tetrahedron acts as the basic building block for the Laves phase [25]. Though it is said that Laves phase is formed exactly at the atomic size ratio 1.225, a slight deviation from this ratio can also form Laves phase. Kuo [26] showed that Ti and Zr form binary Laves phase with Cr, Mn, Fe and Co but not with Cu and Ni (Table 3). The same trend occurs with Hf.

Apart from the binary Laves phases, ternary Laves phases also exist where two atoms of similar atomic size occupy the same site in the crystal lattice. Ternary Laves phase forms in the Zr–Ti–Ni system at $Zr(Ti,Ni)_2$ composition. This phase lies in the vertical section of Ti_2Ni and Zr_2Ni, which have exactly the opposite stoichiometry to the Laves phase. This is isostructural with $MgZn_2$. In this structure, Ti and Ni occupy similar sites. As the atomic size of Hf is very close to that of Zr, it can be postulated that Hf will also form ternary Laves phase with Ti and Ni.

Essentially, anti-Laves phase as stated by Amand and Giessen [27] means A_2B, opposite stoichiometry, i.e. 2:1. At this stoichiometry interesting structures are found. Though it is termed anti-Laves phase, this is a slight misnomer. The structure of anti-Laves phase and that of the Laves phase is not the same. The formation of anti-Laves phases of Ti, Zr, Hf with Cr, Mn, Fe, Co, Ni and Cu is given in Table 4. A typical example is cF96 Ti_2Ni. In addition, tetragonal structures are also found. In some cases metastable cF96 structure is also found, e.g. Zr_2Ni. Cr does not form any anti-Laves phase with Ti, Zr and Hf. This cF96 structure can also be explained by the super-tetrahedron model. In this compound Ni atoms

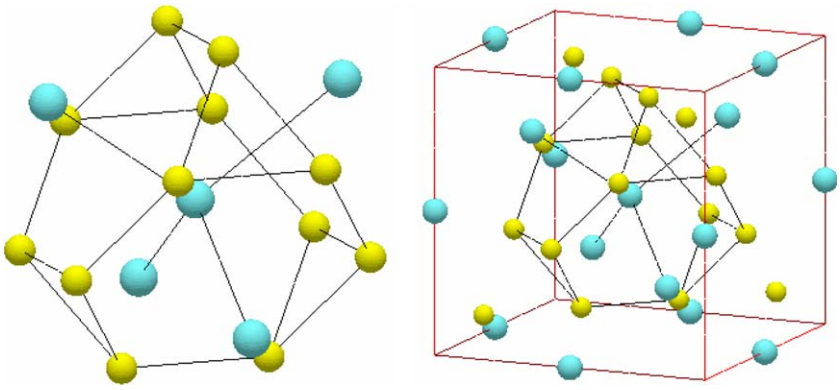

Fig. 10. Structure of the super-tetrahedron, which can be seen as the basic building block for the Laves and anti-Laves phases.

Table 3
Binary Laves phases of Ti, Zr, Hf with Cr, Mn, Fe, Co, Ni and Cu along with their atomic radius ratios

	Cr	Mn	Fe	Co	Ni	Cu
Ti	1.13 $MgCu_2$	1.16 $MgZn_2$	1.17 $MgZn_2$	1.18 $MgCu_2$	1.18 –	1.15 –
Zr	1.23 $MgZn_2$	1.26 $MgZn_2$	1.27 $MgCu_2$	1.28 $MgCu_2$	1.28 –	1.25 –
Hf	1.23 $MgCu_2$ $MgZn_2$	1.21 $MgZn_2$	1.24 $MgCu_2$ $MgZn_2$	1.26 $MgCu_2$	1.27 –	1.24 –

form the tetrahedron and around each Ni atom an icosahedron is formed by the Ti atoms. The only difference between the Laves and the anti-Laves phase lies in the connecting structure. In the Laves phase super-tetrahedra directly penetrate each other. In the case of anti-Laves phase, along the four tetrahedral directions around the Ti atom another icosahedron is formed which acts as a bridge and the voids are filled by octahedra [25]. The structure of a super-tetrahedron is shown in Fig. 10. It can be observed that both the phases have got structural characteristics that can be explained by the Bernal deltahedra and Frank–Kasper polyhedra.

In relation to glass formation it is observed that both Laves and anti-Laves phases are suitable compositions for glass formation. With the advent of bulk metallic glasses it is observed that in the Mg–Ca system Mg can be continuously replaced by calcium and glasses form at both Ca_2Mg and $CaMg_2$ compositions. The radius ratio of Ca and Mg is 1.23. In the present work also extensive formation of anti-Laves phase has been observed. It can be deduced from this observation that glasses form at both Laves and anti-Laves compositions.

Table 4
Stable binary anti-Laves phases of Ti, Zr, Hf with Cr, Mn, Fe, Co, Ni and Cu

	Cr	Mn	Fe	Co	Ni	Cu
Ti	–	–	–	Ti_2Co cF96	Ti_2Ni cF96	Ti_2Cu tI6
Zr	–	–	Zr_2Fe tI12	Zr_2Co tI12	Zr_2Ni tI12	Zr_2Cu tI6
Hf	–	Hf_2Mn cF96	Hf_2Fe cF96	Hf_2Co cF112	Hf_2Ni tI12	Hf_2Cu tI6

5. Conclusions

1. The difference in the glass-forming ability of the alloys has been explained on the basis of atomic size difference and binary heat of mixing. Though Ti, Zr and Hf belong to the same group in the periodic table, their behaviour as regards glass-forming ability is different because of the similar atomic size of Zr and Hf and the much smaller size of Ti.
2. The Ni-bearing alloys precipitate quasicrystals or crystalline phases. The difference in crystallisation behaviour and phase formation has been explained using atomic radius mismatch and heat of mixing of the constituent elements. Mendeleev number can be used in order to classify elements on the basis of their outer electron configuration.
3. The phases precipitated at the initial stages of crystallisation are related to Frank–Kasper phases. The structures of the Laves and the anti-Laves phases can be explained by very similar structural polyhedra, and they have the structural characteristics of glass.

Acknowledgements

The authors acknowledge the collaboration with Professor A. Inoue and Dr. D.V. Louzguine and stimulating discussions with Professors K. Chattopadhyay and V. Jayaram and Ms. Tripti Biswas. Research funding from the Board of Research in Nuclear Sciences (DAEO/MMT/SRG/105) is gratefully acknowledged.

References

[1] Inoue A. Acta Mater 2000;48:279.
[2] Inoue A, Zhang T, Saida J, Matsushita M, Chen MW, Sakurai T. Mater Trans JIM 1999;40:1181.

[3] Loffeler JF, Johnson WL, Wagner W, Thiyagrajan P. Mater Sci Forum 2000;343–346:179.
[4] Altounian Z, Batalla E, Strom-Olsen JO, Walter JL. J Appl Phys 1987;61:149.
[5] Wagner CNJ. In: Luborsky FE, editor. Amorphous metallic alloys. London: Butterworth; 1983. p. 58.
[6] Inoue A, Zhang W, Zhang T, Kurosaka K. Acta Mater 2001;49:2645.
[7] Zhang T, Inoue A, Masumoto T. Mater Sci Eng A 1994;181–182:1423.
[8] Lee GW, Croat TK, Gangopadhyay AK, Kelton KF. Philos Mag Lett 2002;82:199.
[9] Huett VT, Kelton KF. Mater Res Soc Symp Proc 2003;754:359.
[10] Molokanov VV, Petrzhik MI, Mikhailova TN, Sviridova TA, Djakonova NP. J Non-Cryst Solids 1999;250–252:560.
[11] Ma L, Wang L, Zhang T, Inoue A. Mater Trans JIM 2002;43:277.
[12] Kim KB, Warren PJ, Cantor B. Mater Trans JIM 2003;44:411.
[13] Guo X, Louzguine DV, Inoue A. Mater Trans JIM 2001;42:2406.
[14] Ma L, Wang L, Zhang T, Inoue A. Mater Trans JIM 2002;43:2357.
[15] Li C, Saida J, Matsushita M, Inoue A. Philos Mag Lett 2000;80:621.
[16] Pettifor DG. Physica B 1988;149:3.
[17] Semenova EL, Tret'yachenko LA. Powder Metall Metal Ceram 2001;40:414.
[18] Gupta KP. J Phase Equilib 2001;22:73.
[19] Senkov ON, Scott JM. Scripta Mater 2004;50:449.
[20] Inoue A, Saida J, Matsushita M, Sakura T. Mater Trans JIM 2000;41:362.
[21] Li C, Ranganathan S, Inoue A. Acta Mater 2001;49:1903.
[22] Murty BS, Ping DH, Hono K. In: Pathak LC, Venkateswarlu K, Bandhopadhyay A, Roy AK, editors. Advanced materials. New Delhi: Allied Publisher; 2003. p. 40.
[23] Xing LQ, Eckert J, Loser W, Schultz L. Appl Phys Lett 1999;74:664.
[24] Li C, Inoue A. Mater Trans JIM 2001;42:176.
[25] Wang XD, Qi M, Thiel PA, Dong C. Philos Mag 2004;84:825.
[26] Kuo K. Acta Metall 1953;1:720.
[27] Amand RS, Giessen BC. Scripta Metall 1978;12:1021.